Journal of Advanced Ceramics
2019, **8**(3): 377–388
https://doi.org/10.1007/s40145-019-0320-x
ISSN 2226-4108
CN 10-1154/TQ

Research Article

Study of structural, electrical, and photoluminescent properties of $SrCeO_3$ and Sr_2CeO_4

Dharmendra Yadav, Upendra Kumar, Shail Upadhyay*

Department of Physics, *Indian Institute of Technology (BHU)*, *Varanasi 221005*, *India*

Received: October 19, 2018; Revised: January 24, 2019; Accepted: February 9, 2019

Abstract: Phase pure powders of $SrCeO_3$ and Sr_2CeO_4 have been synthesized by calcination at 1000 ℃ for 14 h via solid state ceramic route. Ceramics/pellets of these samples have been obtained by sintering at 1200 ℃ for 12 h. The Rietveld refinement of X-ray diffraction (XRD) pattern of sintered powders confirmed orthorhombic structure of both the samples with space group *Pnma* and *Pbam* for $SrCeO_3$ and Sr_2CeO_4, respectively. Scanning electron microscopic (SEM) studies indicated that both the compounds have dense microstructure, but morphology and size of the grains are different. The impedance spectroscopy technique has been employed to study the relaxation phenomenon. DC conductivity of the samples has been measured in the temperature range of 200–600 ℃ to understand the conduction mechanism. The activation energy for relaxation (E_{relax}) and DC conduction (E_{cond}) are found to be the same for both the compounds. Based on the numerical value of activation energies, relaxation and conduction mechanism in both the samples are attributed to migration of doubly ionized oxygen vacancies ($V_o^{\cdot\cdot}$). Photoluminescence technique has been employed to confirm the existence of oxygen vacancies. These studies have indicated that migration of oxygen vacancies in Sr_2CeO_4 is occurring mainly along *a* and *c* direction, i.e., via perovskite cells. Further, the present work has clearly indicated that besides optical properties, electrical properties of Sr_2CeO_4 are also interesting and can be utilized for various applications such as oxide ion conduction electrolyte in solid oxide fuel cells (SOFCs).

Keywords: Sr_2CeO_4; $SrCeO_3$; impedance spectroscopy; DC conductivity

1 Introduction

In the last two decades, perovskite oxide $SrCeO_3$ has attracted considerable attention due to its potential applications in fuel cell, hydrogen sensor, H_2–D_2 gas cell, etc. [1–4]. Recently it has been investigated as thermal barrier coating candidate for high-temperature applications [5]. It is well known that doped $SrCeO_3$ materials show protonic conduction at elevated temperature under hydrogen-containing atmosphere, which can be used in many electrochemical processes such as hydrogen production, hydrogen sensors, etc. [6–10]. Recently composite electrolytes based on $SrCeO_3$ with high ionic conductivities have been explored for the intermediate temperature fuel cells (ITFCs) [11–13].

Layered perovskite oxide Sr_2CeO_4 with K_2NiF_4-type structure was discovered by Danielson *et al*. [14] in 1998. Sr_2CeO_4 has an orthorhombic crystal structure

* Corresponding author.
E-mail: supadhyay.app@itbhu.ac.in

with one-dimensional chains of edge-sharing CeO_6 octahedrons linked by strontium ions. Undoped Sr_2CeO_4 is a promising blue emitting phosphor characterized by its high thermal and chemical stability and excellent optical properties [15]. Influence of grain size on optical properties of Sr_2CeO_4 has been investigated [16]. Recently studies on scintillation and photoluminescence properties of Sr_2CeO_4 were reported [17]. Photoluminescence (PL) properties of Sr_2CeO_4 doped with Yb^{3+} [18], Sm^{3+} [19], Dy^{3+} [20] and co-doped with Eu^{3+} and Tb^{3+} [21], Eu^{3+} and Dy^{3+} [22], and Eu^{3+} and Gd^{3+} [23] were reported. Tuneable luminescence of Sr_2CeO_4:M^{2+} (M = Ca, Mg, Ba, Zn) and Sr_2CeO_4:Ln^{3+} (Ln = Eu, Dy, Tm) nanophosphors have been studied [22]. Recently studies about anti-Stokes white light generated from undoped [24], Nd^{3+} [25], and Eu^{3+}-doped [26] Sr_2CeO_4 under near infrared excitation were published. It is reported that emission colour of Eu^{3+} doped Sr_2CeO_4 nanophosphors depends on temperatures which make them useful for nanothermometry technology. Eu^{3+} doped Sr_2CeO_4 phosphors emitting white light (by combining blue, green, and red emissions) have potential applications not only in the fields of lamps and display devices under 280 nm excitation, but also in the field of LEDs under near UV (350 nm) excitation [28–30].

It has been found from a thorough literature survey that only one or two published results are available on investigations of the electrical properties of Sr_2CeO_4. A systematic study of the electrical properties of $SrCeO_3$ and Sr_2CeO_4 in a wide temperature and frequency range is still lacking. Moreover, like other A_2BO_4 oxides, Sr_2CeO_4 can be both oxygen-deficient (by generation of oxygen vacancies) and oxygen-excess (by oxygen interstitial). Oxygen ion migration in Sr_2CeO_4 can occur via mechanisms associated with either oxygen vacancies or oxygen interstitials. Therefore, it was considered worthwhile to synthesize $SrCeO_3$ and Sr_2CeO_4 under identical experimental conditions and compare their structural, electrical, and photoluminescent properties.

2 Experimental

2. 1 Materials synthesis

Powder of $SrCeO_3$ and Sr_2CeO_4 was synthesized via the solid state reaction method using $SrCO_3$ (purity of 99.9%, Alfa Aesar) and CeO_2 as raw materials. CeO_2 was obtained by decomposing ammonium cerium nitrate $(NH_4)_2Ce(NO_3)_6$ (purity of 99.5%, Alfa Aesar) at 1000 ℃. Stoichiometric amounts of raw materials together with a known amount of acetone (as mixing media) were milled in a planetary ball-mill (Retsch PM200, Germany) using zirconia balls for 8 h at 200 rpm. The mixtures were dried by keeping them in an oven for overnight. Thermogravimetric (TG) and differential scanning calorimetry (DSC) curves of mixtures were recorded using simultaneous TG-DSC thermal analyzer (Mettler Toledo, Germany), in the temperature range of 30–1000 ℃, with a heating rate of 10 ℃/min in a nitrogen atmosphere. The dried mixtures were calcined in alumina crucibles at different temperatures and time to obtain phase pure powder of desire compounds. Based on the results of TG, the lowest temperature of calcination was decided at 800 ℃ and time of 8 h. Finally, single phase powder of $SrCeO_3$ and Sr_2CeO_4 was obtained by calcination at 1000 ℃ for 14 h. Obtained pure phase powders were mixed with 2 wt% polyvinyl alcohol (PVA) and pressed uniaxially into cylindrical pellets (diameter ~12 mm, thickness ~2 mm) under a load of 5 t using a hydraulic press. These pellets were kept in alumina crucibles and sintered at 1200 ℃ for 12 h in a high-temperature programmable muffle furnace (Matrix, India). Initially, pellets were heated slowly at a rate of 2 ℃/min up to 200 ℃ and maintained at this temperature for 2 h to burn off the binder. The pellets were then heated at a rate of 5 ℃/min to the sintering temperature of 1200 ℃ and kept at this temperature for 12 h. After sintering, the pellets were cooled to 600 ℃ at a rate of 5 ℃/min followed by natural cooling up to room temperature and kept in a desiccator.

2. 2 Materials characterization

The calcined and sintered powders were characterized using an X-ray diffractometer (Miniflex II, Rigaku, Japan) at a scan rate of 2 ℃/min in scanning angles of 20°–80°. To analyze the microstructure and elemental composition of the samples, a scanning electron microscope (EVO18, Zeiss, Germany) coupled with energy-dispersive X-ray (EDX) analyzer was used. The micrographs of the freshly fractured and gold- coated surfaces of the pellets were recorded. For the electrical measurements (impedance and DC conductivity), the sintered pellets were polished using emery papers of different grades. Thereafter, silver (Ag) paste was applied to both sides of the circular faces of the pellets which were then dried at 700 ℃ for 15 min, to be

made conductive. The measurements of real and imaginary parts of the impedance at various temperatures (between 200 and 600 ℃) in the frequency range of 1 Hz–1 MHz was carried out using a high-performance frequency analyzer (Alpha-A, Novocontrol, Germany) with an applied voltage of 20 mV AC signals. DC resistance was measured by applying a voltage of 5 V across the samples from a constant-voltage source using (Model 617 Electrometer, Keithley, USA) two-probe method. The resistance of the samples was measured at different temperatures between 200 and 600 ℃ keeping each temperature constant within ±1 ℃. The photoluminescence (PL) spectrum of sintered powders was recorded with a spectrometer (F-4500, Hitachi, Japan) using a 150 W xenon lamp as a source at a spectral resolution of 5 nm.

3 Results and discussion

3. 1 Thermal analysis (TGA-DSC) of mixture of raw materials

To ensure the temperature required for the reaction between raw materials to form desire compounds, thermogravimetric (TGA) and DSC measurements were carried out. TGA and DSC data of ball milled mixtures of raw materials $SrCO_3$ and CeO_2 for $SrCeO_3$ (1 mole : 1 mole) and Sr_2CeO_4 (2 mole : 1 mole) were recorded up to 1000 ℃ with a heating rate of 10 ℃/min in N_2 gas atmosphere. TGA and DSC curves of mixture for $SrCeO_3$ and Sr_2CeO_4 are shown in Figs. 1(a) and 1(b), respectively. The TG curves show total weight loss approximately 14.48% (for $SrCeO_3$) and 20.41% (for Sr_2CeO_4) in two steps. The first step weight loss observed in the temperature range of 30–100 ℃ may be due to evaporation of remaining acetone or moisture adsorbed on the surface of the particles of the reactants. The second and main weight loss step recorded in the temperature range of 800–970 ℃ is assigned to the expulsion of CO_2 gas during reaction between $SrCO_3$ and CeO_2 according to Eqs. (1) and (2):

$$SrCO_3 + CeO_2 \rightarrow SrCeO_3 + CO_2 \quad (1)$$

$$2SrCO_3 + CeO_2 \rightarrow Sr_2CeO_4 + 2CO_2 \quad (2)$$

The theoretically calculated weight losses for reactions (1) and (2) are approximately 13.76% and 18.83%, respectively. The theoretical and experimental percentage weight losses (in the second step) are approximately the same for both the mixtures and ensure complete expulsion of CO_2 from the product. In the DSC curve of the mixtures for $SrCeO_3$ and Sr_2CeO_4, endothermic peaks at 900 and 950 ℃ were recorded, respectively. Endothermic peaks in the DSC curves may be associated with the formation of desire compounds $SrCeO_3$ and Sr_2CeO_4 according to the reactions (1) and (2). The results obtained by the present work are in agreement with previously reported results [31,32].

3. 2 Structural characterization using XRD

Powder X-ray diffraction (XRD) patterns of the mixtures for $SrCeO_3$ and Sr_2CeO_4 calcined at 1000 ℃ for 14 h are shown in Fig. 2. All the peaks present in the diffraction patterns were indexed to orthorhombic structure of $SrCeO_3$ (JCPDS card No. 47-1687) and Sr_2CeO_4 (JCPDS card No. 89-5546). No peaks corresponding to any impurity phase, intermediate phase and raw materials were seen in the XRD patterns, which confirmed formation of single-phase powder of both the samples.

For microstructural and electrical characterizations, single phase calcined powders were pelletized and sintered at 1200 ℃ for 12 h. The XRD diffraction pattern of sintered powders was recorded and shown in Fig. 3. The XRD patterns of sintered powders and corresponding calcined powders are matching which

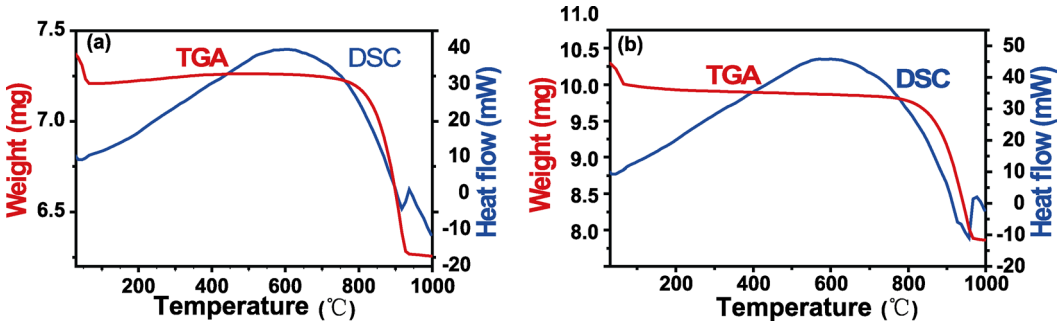

Fig. 1 TGA–DSC curves of stoichiometric mixture of raw materials ($SrCO_3$ and CeO_2) for (a) $SrCeO_3$ and (b) Sr_2CeO_4.

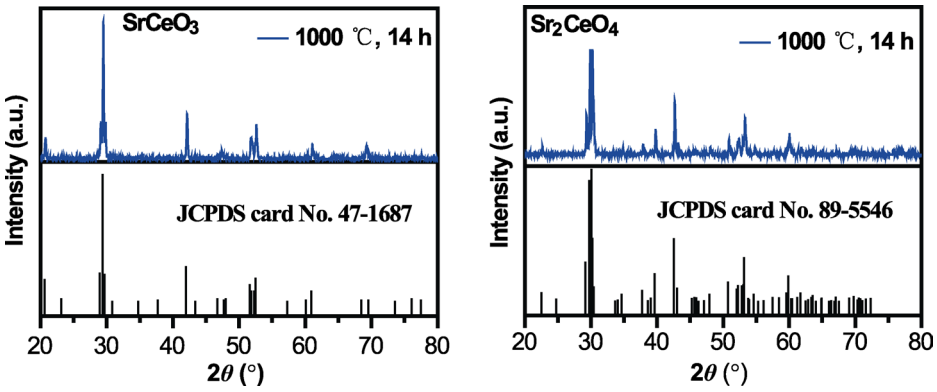

Fig. 2 XRD patterns of calcined powders.

suggest that the evolution of new phases and decomposition of $SrCeO_3$ and Sr_2CeO_4 phases did not occur during prolonging the sintering process. Further, it was noticed that the peaks present in the XRD pattern of the sintered powders are sharper than that in the calcined powders, which confirms grain growth during sintering. The stability of Sr_2CeO_4 phase up to 1200 ℃ disagrees with an earlier report [33] in which powder synthesized by solid state reaction method had stability up to 1100 ℃. It is mentioned that powder synthesized via sol-gel method had phase stability up to 1200 ℃. The XRD pattern of sintered powders was Rietveld refined using Full-Prof software and depicted in Fig. 3. In the Rietveld refinement, the peak profiles were modelled by pseudo-Voigt function by considering six-coefficient polynomial background. The Rietveld refinement was carried out to orthorhombic crystal structure with space group *Pnma* (for $SrCeO_3$) and *Pbam* (for Sr_2CeO_4). The reliability and structural parameters obtained from the refinement are listed in Table 1. The lattice parameters obtained from the refinement agree with the literature values [34].

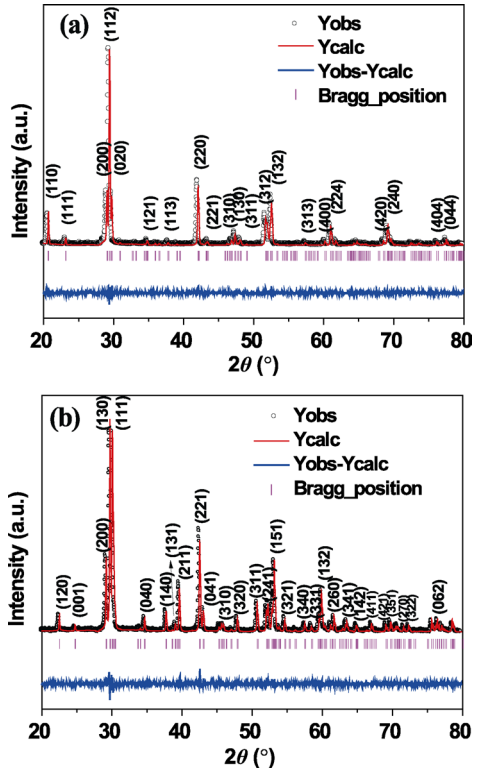

Fig. 3 Rietveld refinement profiles of XRD patterns of sintered powders of (a) $SrCeO_3$ and (b) Sr_2CeO_4.

The experimental density (d_{exp}) of the sintered pellets was calculated using Archimedes' principle. The theoretical density (d_{th}) of the samples was calculated from the molecular weight of the samples and their lattice parameters obtained from the Rietveld analysis. The percentage porosity of the ceramic of the

Table 1 Parameters obtained from Rietveld refinement of XRD data of $SrCeO_3$ and Sr_2CeO_4

$SrCeO_3$	Space group	*Pnma* (62)
	Crystal structure	Orthorhombic
	Lattice parameters (Å)	a = 6.1312 Å, b = 8.5604 Å, c = 5.9946 Å
	Reliability factors	R_P = 17.2, R_{wp} = 16.5, χ^2 = 4.03
	Theoretical density (g/cm^3)	5.72
	Experimental density (g/cm^3)	5.39
	porosity	5%
Sr_2CeO_4	Space group	*Pbam* (55)
	Crystal structure	Orthorhombic
	Lattice parameters (Å)	a = 6.1196 Å, b = 10.3487 Å, c = 3.5972 Å
	Reliability factors	R_P = 15.3, R_{wp} = 16.1, χ^2 = 4.44
	Theoretical density (g/cm^3)	5.42
	Experimental density (g/cm^3)	5.22
	porosity	4%

samples is calculated using the formula:

$$\text{porosity}\ (\%) = \frac{d_{\text{th}} - d_{\text{exp}}}{d_{\text{th}}} \times 100 \qquad (3)$$

The experimental density, theoretical density, and percentage porosity of the samples are mentioned in Table 1. It is noted from Table 1 that the experimental density of the sintered samples is $\geqslant$ 95% of theoretical density which confirms dense microstructure of the samples.

3. 3 Microstructural and compositional analysis

Figure 4 shows scanning electron micrograph (SEM) of fractured surfaces of pellets sintered at 1200 ℃ for 12 h. The SEM images revealed dense structure and well grown grains separated by grain boundaries. It is noted that the morphology of grains of $SrCeO_3$ is spherical and edges are smooth. On the other hand, the morphology of grains of Sr_2CeO_4 is pyramidal with clear edges and facets. The distribution in the grain size is obtained using 'ImageJ' software and presented in the form of a histogram (shown in inset of Fig. 4). The average value of grain size of the samples was obtained by fitting Gaussian function to the distribution of grain sizes as shown in Fig. 4. The average grain size of $SrCeO_3$ and Sr_2CeO_4 is found to be 1.99 and 2.92 μm, respectively. Structure of Sr_2CeO_4 consists of stacking of perovskite layers ($SrCeO_3$) alternating with rock salt like layers (SrO) along the *b*-axis. Due to the layering of SrO, the size of the unit cell of Sr_2CeO_4 is larger than $SrCeO_3$. This may be the reason for larger grain size of Sr_2CeO_4 as compared to $SrCeO_3$. The obtained value of average grain size for both the compounds is consistent with previous reports available in the literature on these oxides [5,33].

Compositional homogeneity (in terms of the concentration profile of the elements) was probed by recording energy dispersive X-ray (EDX) spectra of different regions of the fractured surfaces of the pellets. EDX spectrum of one of the randomly chosen regions is shown in Fig. 5. Figure 5 shows the presence of peaks corresponding to Sr, Ce, and O elements only.

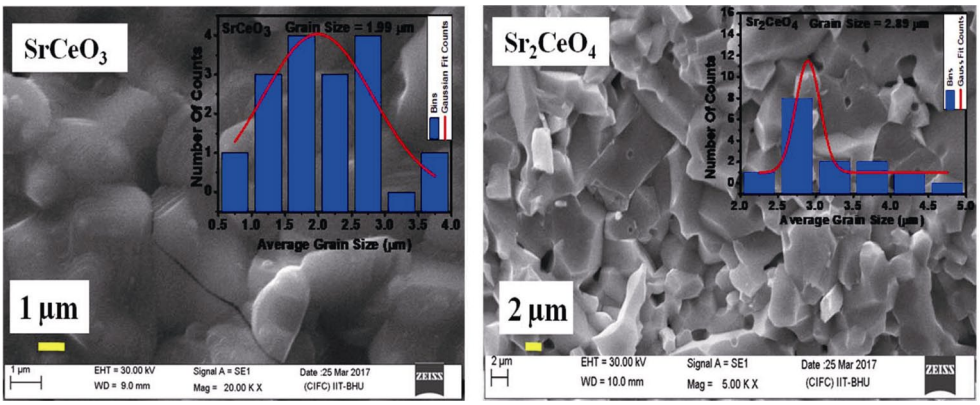

Fig. 4 SEM images of fractured surfaces of sintered pellets.

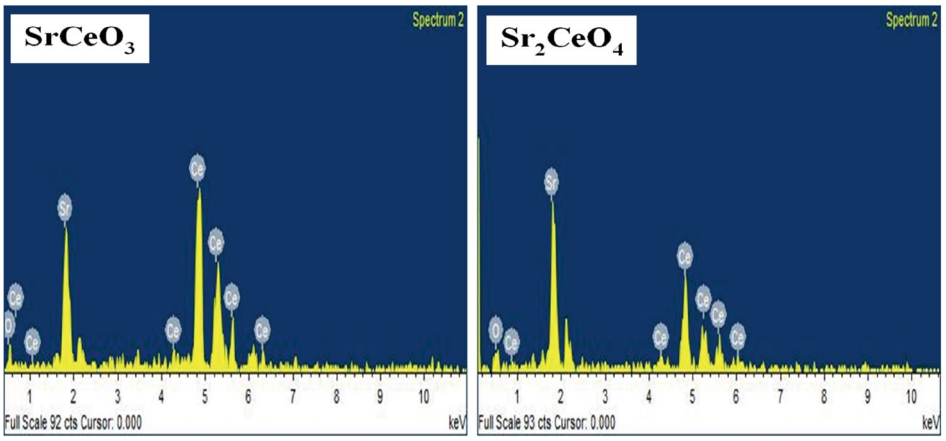

Fig. 5 EDX spectra of fracture surfaces of sintered pellets.

Quantitative data for atomic and weight percentage of the elements present in different regions is as per expected stoichiometry of $SrCeO_3$ and Sr_2CeO_4 ceramics.

3. 4 Electrical characterization

3.4.1 By impedance spectroscopy

Complex impedance spectroscopy is a powerful technique for analyzing the electrical properties of the polycrystalline materials [35]. This technique enables us to separate out the contribution of grain, grain boundary, and sample-electrode interface from the total impedance/resistance of a polycrystalline sample. Impedance data can be presented in two types of plots: (1) complex plane, e.g., Z'' (imaginary component) vs. Z' (real component) and (2) spectroscopy such as Z'' vs. log$f$. Complex plane plot in general reveals information from features like curve shape and intercepts. On the other hand, the spectroscopic plots show the frequency dispersion directly including the location and width of a relaxation peak.

Figure 6 shows complex plane impedance (Nyquist) plots of $SrCeO_3$ and Sr_2CeO_4 at two different temperatures. At low temperatures (< 300 ℃), a straight line is seen, indicating the insulating behavior properties of both the materials. In the plots at higher temperatures (≥ 300 ℃), a large depressed (center lying below the real axis) semicircular arc in the high frequency range and a small tail in the low frequency range are seen. To obtain the value of resistance (R) corresponding to high frequency arc, the impedance data were fitted using a software. The corresponding capacitance (C) was calculated using the formula $\omega\tau = 2\pi f_{max}RC = 1$, f_{max} is the frequency of the maximum of the semicircle, $\omega = 2\pi f_{max}$, and τ is the relaxation time. The value of capacitance is found to be of the order of 10^{-11} F for both the samples. It is reported in Ref. [36] that the capacitance of the gains of many polycrystalline ceramic oxides lies in the range of pF (10^{-12}–10^{-10} F) while that of the grain boundaries in the range of nF (10^{-9}–10^{-8} F). Thus the obtained value of capacitance indicates that the observed high-frequency semicircle can be attributed to the electrical conduction through the bulk (i.e., grain interior).

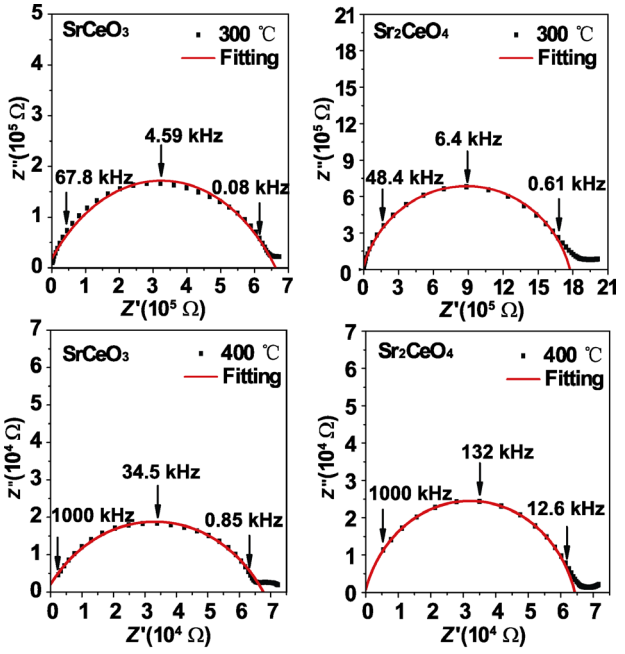

Fig. 6 Complex plane impedance plots (Nyquist plots) of the samples.

To get more information about relaxation phenomenon, impedance data were also represented as spectroscopic plots. Figure 7 shows the variation of the imaginary part of impedance (Z'') as a function of logarithm of frequency at few different temperatures. The Z'' increases with increase in frequency and reaches a maximum value before starts decreasing rapidly. The position of Z'' peak shifts towards higher frequency side with an increase in temperature suggests the existence of a temperature dependent relaxation phenomenon. The relaxation phenomenon in the samples may be due to the presence of defect species. The height of plots of Z'' against log$f$ is proportional to the resistance according to Eq. (4) [37]:

$$Z'' = R\,[\omega\tau / (1+\omega^2\tau^2)] \tag{4}$$

At peak position ($\omega\tau$ = 1), the height of the peak is R/2. Using this approach, values of R at different temperatures were calculated and given in Table 2. The corresponding relaxation frequencies (f_{relax}) and capacitances are also given in Table 2. Variation of R with the inverse of temperature is shown in Fig. 8. Activation energy of conduction (E_{cond}) has been determined using Arrhenius relation and found to be 0.90 and 0.87 eV, for $SrCeO_3$ and Sr_2CeO_4, respectively.

Variation of logτ_{relax} ($\tau_{relax} = 1/f_{relax}$) with the inverse of temperature is shown in Fig. 9. Linear behaviour of logτ_{relax} with 1000/T indicates that relaxation time obeys Arrhenius relation given by Eq. (5):

$$\tau_{relax} = \tau_o \exp(E_{relax}/k_B T) \tag{5}$$

where τ_o is the relaxation time at infinite temperature, E_{relax} is the activation energy for relaxation, k_B is the

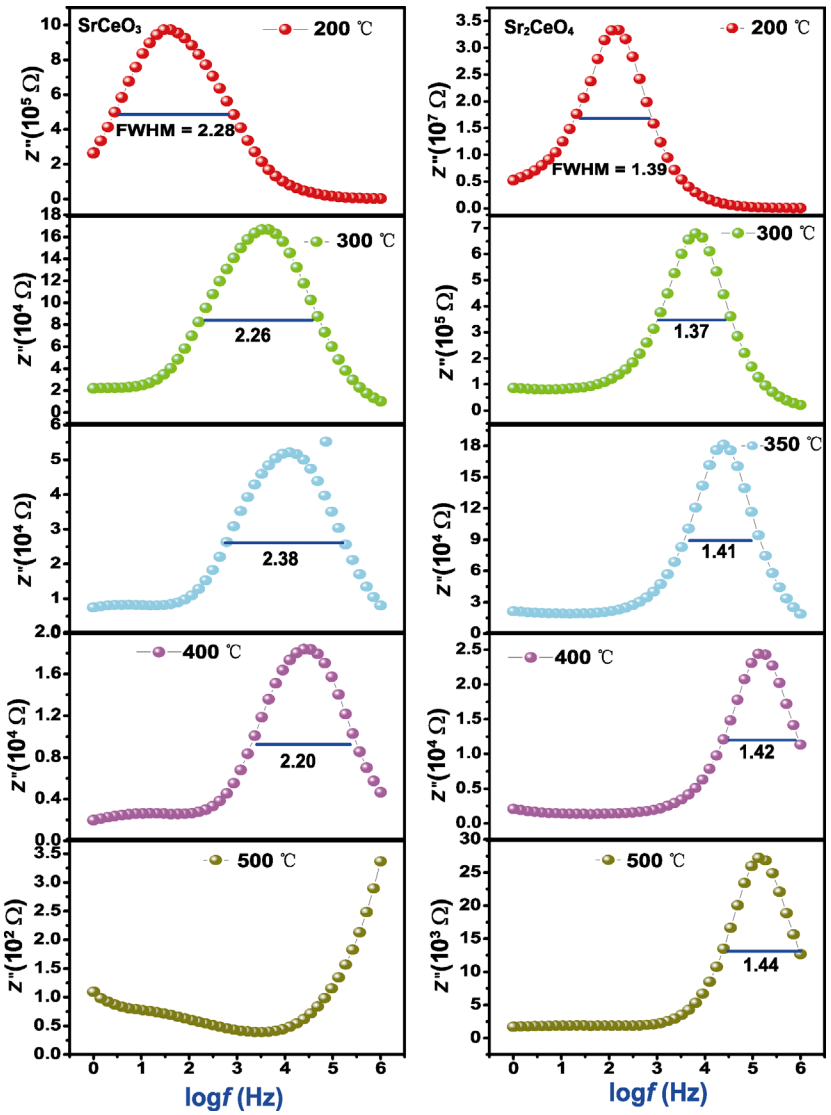

Fig. 7 Variation of imaginary part of impedance (Z'') with logarithm of frequency at different temperatures. FWHM represents the value of the full width at half-maxima.

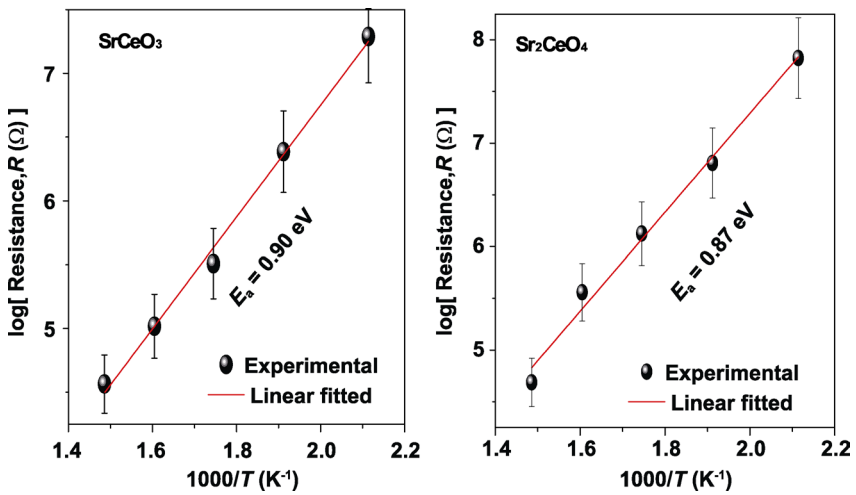

Fig. 8 Variation of logarithm of R with inverse of temperature.

Table 2 Values of relaxation frequency, resistance, and capacitance evaluated from *Z″* vs. log*f* plots

Temperature (℃)	$SrCeO_3$			Sr_2CeO_4		
	Frequency (Hz)	Resistance, R_{total} (Ω)	Capacitance, C_{total} (F)	Frequency (Hz)	Resistance, R_{total} (Ω)	Capacitance, C_{total} (F)
200	41.32	19.44×10^6	1.98×10^{-10}	113.38	6.65×10^7	2.12×10^{-11}
300	3279.6	32.13×10^4	1.51×10^{-10}	6428.1	1.33×10^6	1.86×10^{-11}
350	12,599	10.40×10^4	1.21×10^{-10}	24,694	3.62×10^5	1.78×10^{-11}
400	34,572	3.66×10^4	1.26×10^{-10}	132,810	4.87×10^4	2.46×10^{-11}
500	600,000	7.01×10^3	1.12×10^{-10}	423,455	54.44×10^3	2.20×10^{-11}

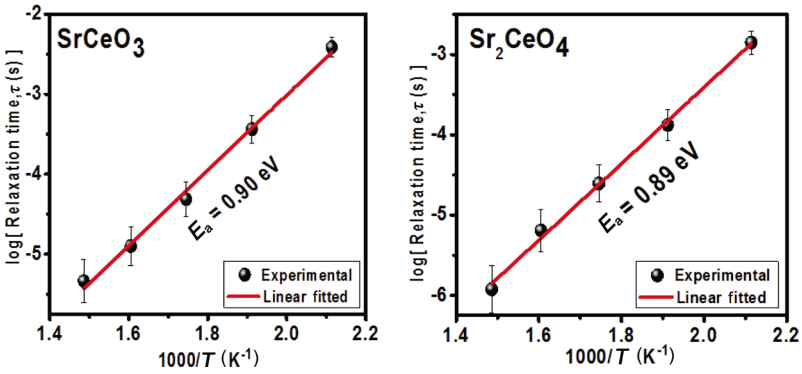

Fig. 9 Variation of logarithm of relaxation time of grain (τ_g) with inverse of temperature.

Boltzmann's constant and T is the absolute temperature. A linear fit of the $\log\tau_{relax}$ vs. $1000/T$ plot has been used to estimate the activation energy of relaxation process of the samples. The value of activation energy obtained from $\log\tau_{relax}$ vs. $1000/T$ and $\log R$ vs. $1000/T$ plots is the same for both the samples. This result shows that mechanism of electrical conduction and relaxation in both the samples is the same. In other words, the same charge specie is involved in relaxation and conduction.

The value of the full width at half-maxima (FWHM) of the peaks shown in Fig. 7 is larger than 1.144 decades (for ideal Debye-type relaxation) for both the samples. This shows a presence of non-Debye nature of the relaxation phenomenon in both the samples. The value of FWHM is 2.44 and 1.30 decades for $SrCeO_3$ and Sr_2CeO_4, respectively. Relaxation peak may be wide either due to overlapping of two peaks/or a single peak originating from a wide distribution of relaxation time due to a variety of energy barriers resulting from local defects. In the microstructure of $SrCeO_3$, grain boundaries are distinctly visible, but not in the microstructure of Sr_2CeO_4 (Fig. 4). Therefore, it is proposed that broad peak is case of $SrCeO_3$ due to overlapping of peak corresponding to grain and grain boundaries. On the other hand, in case of Sr_2CeO_4 slightly higher value of FWHM than the ideal Debye relaxation is due to distribution of relaxation time within the grains.

3.4.2 By DC conductivity measurements

The theoretical density (d_{th}) of the samples was calculated from the molecular weight of the samples and their lattice parameters obtained from the Rietveld analysis.

Due to the limited range of the available multimeter and high values of the DC resistance of the samples, experimental data below 200 ℃ could not be collected. The DC resistances of both the samples were measured in the temperature range of 200–600 ℃ by two-probe method. The DC conductivity (σ_{dc}) of the samples was calculated from the measured resistances and geometrical parameters (thickness and diameter) of the pellet. The plot of $\log\sigma_{dc}$ vs. $1000/T$ for both the samples is shown in Fig. 10. A linear variation is observed between σ_{dc} and $1000/T$ which confirms Arrhenius relationship given below

$$\sigma_{dc} = \sigma_o \exp(-E_{cond}/k_B T) \quad (6)$$

where σ_o is a constant, k_B is Boltzmann's constant and E_{cond} is the activation energy of the DC conduction. The value of E_{cond} for both the samples is obtained by least-square fitting of the conductivity data and found to be 0.89 and 0.87 for $SrCeO_3$ and Sr_2CeO_4, respectively. It is noticed that the numerical value of DC conductivity of Sr_2CeO_4 is slightly lower than that

of $SrCeO_3$ at the same temperatures. Observed order of DC conductivity and corresponding activation energy of the samples agree with earlier studies on electrical properties of these oxides [38,39]. It is well known that doubly ionized oxygen vacancy ($V_o^{\cdot\cdot}$) is the most mobile defect charge specie in the perovskite oxides and doped and undoped ceria oxides. The typical value of the activation energy for the migration of $V_o^{\cdot\cdot}$ lies in the range of 0.55–1.30 eV [40–42]. The obtained values of the activation energy for DC conduction of $SrCeO_3$ and Sr_2CeO_4 fall in this range; therefore, conduction in these samples is ascribed to the migration of doubly ionized oxygen vacancies ($V_o^{\cdot\cdot}$). Formation of oxygen vacancies in these samples could have taken place during sintering at high temperature (1200 ℃). Layered perovskite oxides, A_2BO_4, are reported to accommodate oxygen ions at interstitial sites which is also not possible in the perovskite structure [43]. Therefore, in Sr_2CeO_4, oxygen transport may occur via interstitial migration in the rock-salt (Sr–O) layers and vacancy migration in the perovskite planes ($SrCeO_3$). Almost the same value of the activation energy for both the samples $SrCeO_3$ and Sr_2CeO_4 suggest that conduction in the layered perovskite Sr_2CeO_4 is occurring via oxygen vacancies ($V_o^{\cdot\cdot}$) migration in the perovskite planes ($SrCeO_3$).

The value of activation energy obtained from Figs. 8 and 9 when compared with value of the activation energy obtained from DC conductivity measurement (Fig. 10), is seen to have the same value within the experimental error for both the samples. The same value of the activation energy from both the methods suggest that bulk contribution is dominating in electrical conduction; contribution of grain boundaries and the electrode-ceramic interface is almost negligible particularly for Sr_2CeO_4. Further, the activation energy values suggest that the relaxation process and conduction mechanism in both the samples are of similar source.

3.5 Photoluminescence studies to confirm the presence of oxygen vacancies

Presence of oxygen vacancies in various oxides have been revealed by measuring PL properties [44]. PL emission spectra of both the samples was recorded (exciting with a source of wavelength 280 nm) which are shown in Fig. 11. Presence of a broad emission peak in the range of 425–550 nm in the PL spectrum of Sr_2CeO_4 is consistent with Refs. [15,16]. PL spectra of $SrCeO_3$ were compared with spectra of Sm^{3+} doped $SrCeO_3$ [45]. The difference in the shape of the PL spectrum of $SrCeO_3$ and Sr_2CeO_4 may be due to the difference in the co-ordination number of Sr in their unit cell. The emission peak of $SrCeO_3$ was deconvoluted into three peaks centred at 441 nm (2.81 eV), 462 nm (2.69 eV), and 502 nm (2.47 eV). Whereas the peak in the PL spectrum of Sr_2CeO_4 was deconvoluted into three peaks centred at 448 nm (2.77 eV), 479 nm (2.59 eV), and 520 nm (2.39 eV) as shown in Fig. 11. Based on Ref. [44], peak 1 and 2 are the characteristic emission peaks while peak 3 is assigned to the presence of defect, i.e., oxygen vacancies. Various authors have ascribed the peak around 520 nm (2.40 eV) to the energy level of doubly ionized oxygen vacancies [44].

4 Conclusions

The Rietveld refinement of XRD data of sintered powders confirmed orthorhombic structure and space group *Pnma* and *Pbam* for $SrCeO_3$ and Sr_2CeO_4, respectively. Solid state reaction method synthesized Sr_2CeO_4 phase is stable up to 1200 ℃. SEM studies indicated that both the compounds have dense microstructure, but morphology and size of the grains are different for $SrCeO_3$ and Sr_2CeO_4. Impedance

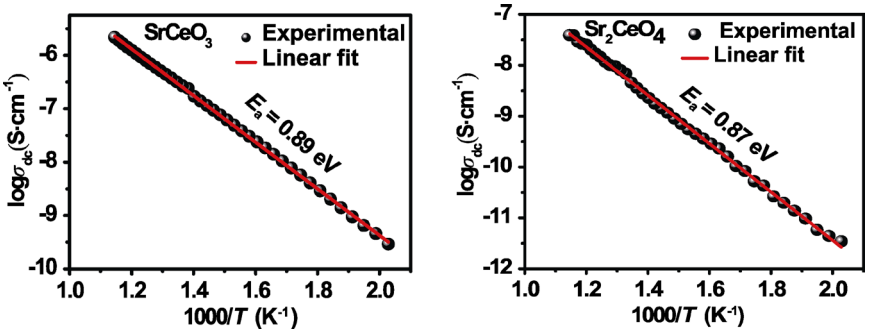

Fig. 10 Variation of logarithm of DC conductivity (σ_{dc}) with inverse of temperature.

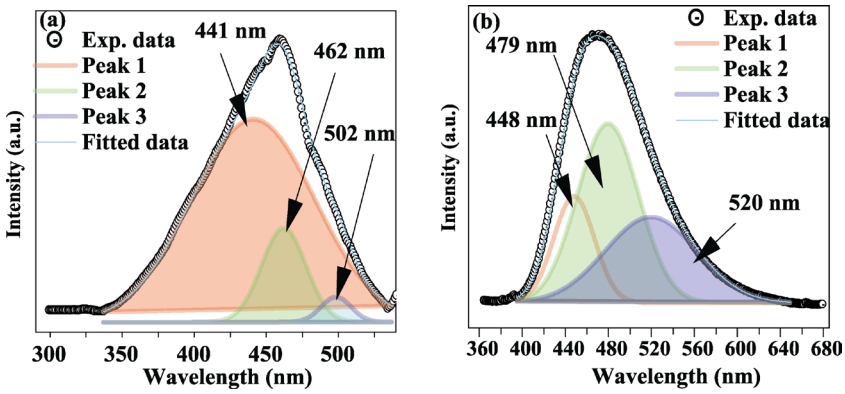

Fig. 11 Emission spectra of sintered samples of (a) $SrCeO_3$ and (b) Sr_2CeO_4.

analysis confirmed presence of single non-Debye type relaxation phenomena in both the samples. The activation energy for relaxation time (E_{relax}) and the activation energy for DC conduction (E_{cond}) is the same for both the samples. Based on the numerical value of activation energies, relaxation and conduction mechanism in both the compounds are assigned to migration of doubly ionized oxygen vacancies ($V_o^{\cdot\cdot}$). Almost the same value of the activation energy for DC conduction of $SrCeO_3$ and Sr_2CeO_4 confirmed that migration of oxygen in Sr_2CeO_4 is occurring in AC plane. PL technique confirmed presence of oxygen vacancies in both the compounds. The present investigation has clearly indicated that besides optical properties, electrical properties of Sr_2CeO_4 are also interesting and can be utilized for various applications. Order of DC conductivity and activation energy of Sr_2CeO_4 is approximately the same as of popular oxide ion conductor CeO_2 electrolyte. By choosing suitable dopants for Sr and Ce sites of Sr_2CeO_4, this oxide can also be a candidate for electrolyte in SOFC application.

Acknowledgements

The authors are grateful to the Head, Department of Physics and Coordinator, Central Instrument Facility Centre (CIFC) and Co-ordination, Centre for energy research and development (CRED), IIT(BHU), Varanasi for providing the experimental facilities required for the characterization of samples. Dharmendra Yadav and Upendra Kumar are thankful to the Ministry of Human Resource and Development (MHRD), the Government of India and co-ordinator for the financial support in terms of Senior Research Fellowship (SRF).

References

[1] Iwahara H, Esaka T, Uchida H, *et al*. Proton conduction in sintered oxides and its application to steam electrolysis for hydrogen production. *Solid State Ionics* 1981, **3–4**: 359–363.

[2] Uchida H. Relation between proton and hole conduction in $SrCeO_3$-based solid electrolytes under water-containing atmospheres at high temperatures. *Solid State Ionics* 1983, **11**: 117–124.

[3] Uchida H, Kimura H, Iwahara H. Limiting current in a high-temperature hydrogen pump with a $SrCeO_3$-based proton conductor. *J Appl Electrochem* 1990, **20**: 390–394.

[4] de vries K J. Electrical and mechanical properties of proton conducting $SrCe_{0.95}Yb_{0.05}O_{3-\alpha}$. *Solid State Ionics* 1997, **100**: 193–200.

[5] Yuan JY, Sun JB, Wang JS, *et al*. $SrCeO_3$ as a novel thermal barrier coating candidate for high–temperature applications. *J Alloys Compd* 2018, **740**: 519–528.

[6] Liu C, Huang JJ, Fu YP, *et al*. Effect of potassium substituted for A-site of $SrCe_{0.95}Y_{0.05}O_3$ on microstructure, conductivity and chemical stability. *Ceram Int* 2015, **41**: 2948–2954.

[7] Sammes N, Phillips R, Smirnova A. Proton conductivity in stoichiometric and sub-stoichiometric yittrium doped $SrCeO_3$ ceramic electrolytes. *J Power Sources* 2004, **134**: 153–159.

[8] Okuyama Y, Isa K, Lee YS, *et al*. Incorporation and conduction of proton in $SrCe_{0.9-x}Zr_xY_{0.1}O_{3-\delta}$. *Solid State Ionics* 2015, **275**: 35–38.

[9] Zhang C, Li S, Liu XP, *et al*. Low temperature synthesis of Yb doped $SrCeO_3$ powders by gel combustion process. *Int J Hydrog Energy* 2013, **38**: 12921–12926.

[10] Yuan WH, Xiao CC, Li L. Hydrogen permeation and chemical stability of In-doped $SrCe_{0.95}Tm_{0.05}O_{3-\delta}$ membranes. *J Alloys Compd* 2014, **616**: 142–147.

[11] Shabanikia A, Javanbakht M, Amoli HS, *et al*. Polybenzimidazole/strontium cerate nanocomposites with enhanced proton conductivity for proton exchange membrane fuel cells operating at high temperature. *Electrochimica*

Acta 2015, **154**: 370–378.

[12] Guan QM, Wang HT, Miao H, *et al*. Synthesis and conductivity of strontium cerate doped by erbium oxide and its composite electrolyte for intermediate temperature fuel cell. *Ceram Int* 2017, **43**: 9317–9321.

[13] Sun L, Miao H, Wang HT. Novel $SrCe_{1-x}Yb_xO_{3-\alpha}$-(Na/K)Cl composite electrolytes for intermediate temperature solid oxide fuel cells. *Solid State Ionics* 2017, **311**: 41–45.

[14] Danielson E, Devenney M, Giaquinta DM, *et al*. X-ray powder structure of Sr_2CeO_4: A new luminescent material discovered by combinatorial chemistry. *J Mol Struct* 1998, **470**: 229–235.

[15] Stefanski M, Marciniak L, Hreniak D, *et al*. Influence of grain size on optical properties of Sr_2CeO_4 nanocrystals. *J Chem Phys* 2015, **142**: 184701.

[16] Seo YW, Noh HM, Moon BK, *et al*. Structural and luminescent properties of blue-emitting Sr_2CeO_4 phosphors by high-energy ball milling method. *Ceram Int* 2015, **41**: 1249–1254.

[17] Kato T, Kawano N, Okada G, *et al*. Scintillation and photoluminescence properties of Sr_2CeO_4 ceramics. *Opt Mater* 2019, **87**: 139–144.

[18] Zhou R, Wei XT, Chen YH, *et al*. Ultraviolet to near-infrared downconversion in Yb^{3+}-doped Sr_2CeO_4. *Phys Status Solidi B* 2012, **249**: 818–823.

[19] Rakov N, Guimarães RB, MacIel GS. Strong infrared-to-visible frequency upconversion in Er^{3+}-doped Sr_2CeO_4 powders. *J Lumin* 2011, **131**: 342–346.

[20] Zhang CX, Shi JS, Yang XJ, *et al*. Preparation, characterization and luminescence of Sm^{3+} or Eu^{3+} doped Sr_2CeO_4 by a modified sol-gel method. *J Rare Earths* 2010, **28**: 513–518.

[21] Monika DL, Nagabhushana H, Krishna RH, *et al*. Synthesis and photoluminescence properties of a novel Sr_2CeO_4:Dy^{3+} nanophosphor with enhanced brightness by Li^+ co-doping. *RSC Adv* 2014, **4**: 38655–38662.

[22] Li J, Li X, Hu SL, *et al*. Photoluminescence mechanisms of color-tunable Sr_2CeO_4:Eu^{3+}, Dy^{3+} phosphors based on experimental and first-principles investigation. *Opt Mater* 2013, **35**: 2309–2313.

[23] Suresh K, Murthy KVR, Atchyutha Rao C, *et al*. Synthesis and characterization of nano Sr_2CeO_4 doped with Eu and Gd phosphor. *J Lumin* 2013, **133**: 96–101.

[24] Grzyb T, Szczeszak A, Rozowska J, *et al*. Tunable luminescence of Sr_2CeO_4:M^{2+} (M = Ca, Mg, Ba, Zn) and Sr_2CeO_4:Ln^{3+} (Ln = Eu, Dy, Tm) nanophosphors. *J Phys Chem C* 2012 **116**: 3219–3226.

[25] Strek W, Tomala R, Marciniak L, *et al*. Broadband anti-Stokes white emission of Sr_2CeO_4 nanocrystals induced by laser irradiation. *Phys Chem Chem Phys* 2016, **18**: 27921–27927.

[26] Stefanski M, Lukaszewicz M, Hreniak D, *et al*. Broadband laser induced white emission observed from Nd^{3+} doped Sr_2CeO_4 nanocrystals. *J Lumin* 2017, **192**: 243–249.

[27] Stefanski M, Marciniak L, Hreniak D, *et al*. Size and temperature dependence of optical properties of Eu^{3+}: Sr_2CeO_4 nanocrystals for their application in luminescence thermometry. *Mater Res Bull* 2016, **76**: 133–139.

[28] Shi LL, Zhang HJ, Li CY, *et al*. Eu^{3+} doped Sr_2CeO_4 phosphors for thermometry: Single-color or two-color fluorescence based temperature characterization. *RSC Adv* 2011, **1**: 298.

[29] Vlasic A, Sevic D, Rabasovic MS, *et al*. Effects of temperature and pressure on luminescent properties of Sr_2CeO_4:Eu^{3+} nanophosphor. *J Lumin* 2018, **199**: 285–292.

[30] Stefanski M, Lukaszewicz M, Hreniak D, *et al*. Laser induced white emission generated by infrared excitation from Eu^{3+}:Sr_2CeO_4 nanocrystals. *J Chem Phys* 2017, **146**: 104705.

[31] Zhang CX, Jiang WJ, Yang XJ, *et al*. Synthesis and luminescent property of Sr_2CeO_4 phosphor via EDTA-complexing process. *J Alloys Compd* 2009, **474**: 287–291.

[32] Zambare PZ. *Synthesis and Characterization of Trivalent (Er^{3+},Tb^{3+}) Doped with Sr_2CeO_4 Phoshor*. Raleigh (USA): Lulu Publication, 2017: 64–65.

[33] Sahu M, Krishnan K, Nagar BK, *et al*. Heat capacity and thermal expansion coefficient of $SrCeO_3$(s) and Sr_2CeO_4(s). *Thermochimica Acta* 2011, **525**: 167–176.

[34] Lu CH, Chen CT. Luminescent characteristics and microstructures of Sr_2CeO_4 phosphors prepared via sol–gel and solid-state reaction routes. *J Sol-Gel Sci Technol* 2007, **43**: 179–185.

[35] Macdonald JR, Johnson WB. Fundamentals of impedance spectroscopy. In *Impedance Spectroscopy: Theory, Experiment, and Applications*. 2nd edn. Barsoukov E, Macdonald JS, Eds. New York: John Wiley & Sons, 2005.

[36] Hodge IM, Ingram MD, West AR. Impedance and modulus spectroscopy of polycrystalline solid electrolytes. *J Electroanal Chem Interfacial Electrochem* 1976, **74**: 125–143.

[37] Upadhyay SHAIL. High temperature impedance spectroscopy of barium stannate, $BaSnO_3$. *Bull Mater Sci* 2013, **36**: 1019–1036.

[38] Ricciardiello F, Sbaizero O, Minichelli D. X-ray characterization and electrical properties of $SrCeO_3$–$SrZrO_3$ solid solution. *Mater Chem Phys* 1984, **10**: 487–497.

[39] Talik E, Lipińska L, Skrzypek D, *et al*. Electronic structure analysis and properties of Sr_2CeO_4 grown by sol–gel method. *Mater Res Bull* 2012, **47**: 3107–3113.

[40] Walsh A, Catlow CRA, Smith AGH, *et al*. Strontium migration assisted by oxygen vacancies in $SrTiO_3$ from classical and quantum mechanical simulations. *Phys Rev B* 2011, **83**: 220301.

[41] Warren WL, Vanheusden K, Dimos D, *et al*. Oxygen vacancy motion in perovskite oxides. *J Am Ceram Soc* 1996, **79**: 536–538.

[42] Kudo T, Obayashi H. Mixed electrical conduction in the fluorite-Type $Ce_{1-x}Gd_xO_{2-x/2}$. *J Electrochem Soc* 1976,

123: 415–419.

[43] Lee D, Lee H. Controlling oxygen mobility in Ruddlesden–Popper oxides. *Materials* 2017, **10**: 368.

[44] Choudhury B, Chetri P, Choudhury A. Annealing temperature and oxygen-vacancy-dependent variation of lattice strain, band gap and luminescence properties of CeO_2 nanoparticles. *J Exp Nanosci* 2015, **10**: 103–114.

[45] Wei L, Yang DM, Hu WY, *et al*. Synthesis and luminescence properties of red phosphor $SrCeO_3:Sm^{3+}$. *J Synth Cryst* 2012, **41**(1): 64–68, 84. (in Chinese)